Mechanistic Insights into the Lithiation and Delithiation of Iron-Doped Zinc Oxide: The Nucleation Site Model

Jakob Asenbauer,[⊥] Alexander Hoefling,[*,⊥] Sylvio Indris, Jens Tübke, Stefano Passerini, and Dominic Bresser[*]

ABSTRACT: The detailed mechanistic understanding of the electrochemical reactions occurring in lithium-ion battery electrodes is fundamental for their further improvement. Conversion/alloying materials (CAMs), such as $Zn_{0.9}Fe_{0.1}O$, one of the most recent alternatives for classic graphite anodes, offer superior specific capacity and rate capability. However, despite fast kinetics, CAMs suffer from a large voltage hysteresis upon de-/lithiation and improvable Coulombic efficiencies when cycled in a large voltage window. Here, we use isothermal microcalorimetry together with operando X-ray diffraction as well as ex situ ^{7}Li NMR and ^{57}Fe Mössbauer spectroscopies to investigate the asymmetric reaction mechanism of the lithiation and delithiation of $Zn_{0.9}Fe_{0.1}O$ during electrochemical cycling. We demonstrate that the measured heat flow is correlated with compositional changes of the electrode material. This combination of highly complementary techniques allows us to propose a new nucleation site model for the initial lithiation of $Zn_{0.9}Fe_{0.1}O$. Modeling the heat flow provides concrete evidence for the deleterious impact of high anodic cutoff potentials (>2 V), resulting in a continuous quasireversible solid electrolyte interphase formation. The presented methodology is suggested to provide improved insights into the reaction mechanism of conversion- and alloying-type energy-storage materials.

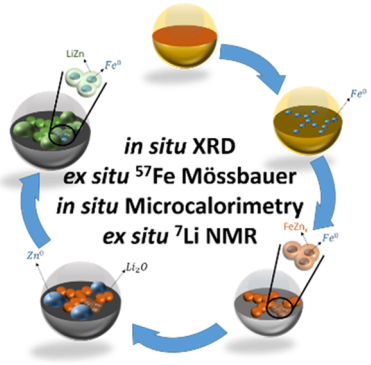

KEYWORDS: *isothermal microcalorimetry, operando XRD, ex situ ^{7}Li NMR, conversion/alloying anodes, lithium-ion batteries*

1. INTRODUCTION

Due to their high power and energy density, Li-ion batteries (LIBs) are the dominant energy-storage technology for portable electronics and increasingly also for large-scale applications like electric vehicles (EVs) and grid storage.[1] Nevertheless, there is still a need for improvement in energy and, especially, power density, in particular for their application in EVs and other transportation applications.[2] Conventional LIBs comprise graphite as the anode material, which is environmentally friendly and has a low de-/lithiation potential, thus offering the aforementioned high energy density.[3] However, its slow lithiation kinetics intrinsically hinder fast charging, particularly at low temperatures.[4] Not least, for this reason, researchers are trying to find alternative anode materials for high-power applications while ideally maintaining a high energy density. Generally, there are two classes of materials that could potentially provide both high(er) capacities and improved rate capabilities: (i) Alloying materials like post-transition metals or metalloids, which can reversibly alloy with lithium during the dis-/charge reaction[5,6] and (ii) conversion materials like transition-metal (TM) oxides, which are reversibly reduced to the corresponding TM nanograins within the simultaneously formed Li_2O matrix.[7,8] Recently, a third class of electrochemically active compounds, referred to as conversion-alloying materials (CAMs), has been attracting the attention of the scientific community.[9] For this class of materials, both the alloying and conversion mechanisms are combined in one single material. One of the most investigated CAMs is certainly $Zn_{0.9}Fe_{0.1}O$.[10−14] The incorporation of the Fe dopant enables substantially increased capacities compared to pure ZnO and a dramatically enhanced cycling stability when coupled with the application of a carbonaceous coating.[15] Nevertheless, there are two main challenges remaining, specifically the rather pronounced voltage hysteresis and the relatively lower Coulombic efficiency, resulting in lower energy efficiencies than graphite-based LIBs.[16] These energy losses are supposed to lead to significant heat generation during the electrochemical reaction. Accordingly, the most suitable technique to investigate such heat changes, originating from the electrochemical processes occurring, is operando isothermal microcalorimetry (IMC). For this nondestructive analysis method, also termed "electrochemical calorimetry", a heat flow calorimeter is coupled with a potentiostat/galvanostat. Its general suitability has been proven already for several lithium insertion/intercalation materials such as $LiCoO_2$,[17] $LiMn_2O_4$,[18−20] $LiNiO_2$,[21] Li-

$[Li_{1/5}Ni_{1/5}Mn_{3/5}]O_2$,[22] $Li_{1+x}[Ni_{1/3}Co_{1/3}Mn_{1/3}]_{1-x}O_2$,[23] $LiNi_{0.8}Co_{0.15}Al_{0.05}O_2$,[24] $LiNi_{0.8}Co_{0.2}O$,[25] graphitic carbon,[17,26] and $Li_{4/3}Ti_{5/3}O_4$.[27] The characteristic heat flow profiles allowed for the evaluation of the underlying insertion/intercalation mechanism and phase changes during de-/lithiation. In addition, IMC offers access to the determination of parasitic heat from decomposition reactions inside the cell. Thus, the stability of different electrolyte compositions[28−30] as well as the effect of certain electrolyte additives[31] and cutoff potentials[32] has been investigated. For active materials storing lithium by alternative mechanisms, however, only very few studies have been reported so far. Seo et al.,[33] for instance, investigated lithium/sulfur cells and found a characteristic heat flow in accordance with the voltage profile that indicated the different phase transitions during discharge. Nonetheless, they considered only the reversible and irreversible heat contributions from the Faradaic reactions, which led to a poor match of the calculated and experimentally observed heat generation rates at relatively lower states of discharge. More recently, Huie et al.[34,35] studied the lithiation process of conversion-type magnetite (Fe_3O_4). They discovered that the measured heat generation rate above 0.86 V could be described by polarization and changes in entropy only. Above that value, an increased heat flow was observed, indicating electrolyte decomposition reactions. Operando X-ray absorption spectroscopy (XAS) supported the onset of solid electrolyte interphase (SEI) formation at such voltage, emphasizing the great potential of IMC for the identification of the different electrochemical processes in energy-storage materials.

Here, we present the thermal characteristics, determined operando by IMC, of carbon-coated iron-doped zinc oxide ($Zn_{0.9}Fe_{0.1}O$−C) as conversion/alloying-type energy-storage material. The characteristic heat flow profile displays precisely the formation of every single phase in the electrode in accordance with the findings obtained by operando X-ray diffraction (XRD) as well as ex situ ^{7}Li NMR and ^{57}Fe Mössbauer spectroscopies. Thereupon, more detailed insights into the electrochemical processes during galvanostatic cycling are obtained. Especially, the separation of the different heat sources by modeling the contributions to the heat flow from polarization and entropic changes revealed that parasitic reactions occur particularly above a threshold of 55% state of discharge (SOD) during lithiation and 80% state of charge (SOC) during delithiation. This comprehensive approach allows for a better understanding of the de-/lithiation mechanism in CAMs and demonstrates the powerful strength and complementarity of IMC for the investigation of advanced energy-storage materials.

2. EXPERIMENTAL SECTION

2.1. Synthesis. The synthesis of carbon-coated $Zn_{0.9}Fe_{0.1}O$ ($Zn_{0.9}Fe_{0.1}O$−C) was performed as reported earlier.[15] Briefly, zinc(II) gluconate hydrate (ABCR) and iron(II) gluconate dihydrate (Aldrich) were dissolved in an aqueous sucrose solution in the required stoichiometric ratio. The water was evaporated at 160 °C, and the remaining precursor was calcined at 450 °C under air. For the carbon coating, 1 g of $Zn_{0.9}Fe_{0.1}O$ was mixed with 0.5 g of sucrose. The mixture was homogenized by planetary ball-milling and subsequently dried at 80 °C prior to a thermal treatment at 500 °C for 4 h under an argon atmosphere.

2.2. Electrode Preparation and Cell Assembly. Electrodes were prepared by adding the active material and carbon black (Super C65, Imerys) to a 1.25 wt % solution of sodium carboxymethyl cellulose (CMC, Dow Wolff Cellulosics) in ultrapure water. The composition of the dry material was 75 wt % $Zn_{0.9}Fe_{0.1}O$−C, 20 wt % carbon black, and 5 wt % CMC binder. The slurry was homogenized by ball-milling for 2 h, subsequently cast on a dendritic copper foil (Schlenk), and dried overnight at room temperature. Disc electrodes with 12 mm diameter were punched and dried at 120 °C under vacuum (<10 ^{3} mbar) overnight. For the electrochemical characterization and IMC measurements, two-electrode coin cells (Hohsen) were assembled in an argon-filled glovebox employing lithium metal (Honjo, battery grade) as the counter and reference electrode and a sheet of Whatman glass fiber as the separator; the latter was soaked with a 1 M solution of $LiPF_6$ in a mixture of ethylene carbonate (EC) and dimethyl carbonate (DMC) (EC/DMC 1:1 w/w).

2.3. Operando XRD. Operando X-ray diffraction (XRD) upon de-/lithiation was performed using a self-designed two-electrode in situ cell.[36] The electrode slurry, which had the same composition as mentioned above (75 wt % $Zn_{0.9}Fe_{0.1}O$−C, 20 wt % Super C65, and 5 wt % CMC binder), was homogenized by manual grinding in an Agate mortar and directly cast on a beryllium (Be) disc (25 mm diameter, 0.25 mm thick), which served simultaneously as the current collector and the "window" for the X-ray beam. The coated Be disc was dried for 4 h at room temperature and at 60 °C under vacuum overnight. A 19 mm glass fiber disc (Whatman), drenched with 300 μL of the electrolyte (1 M $LiPF_6$ in EC:DEC 3:7 w/w), was used as the separator, and metallic lithium (Honjo, battery grade) served as the counter and reference electrode. X-ray diffractograms were recorded using a Bruker D8 Advance diffractometer (Cu Kα radiation, λ = 0.154 nm) within the 2θ range of $25 \leq 2\theta \leq 65°$.

2.4. Ex Situ ^{7}Li NMR and Mössbauer Analysis. For the ex situ ^{7}Li NMR and Mössbauer investigation, $Zn_{0.9}Fe_{0.1}O$−C was mixed with Super C65 in a ratio of 75:20 and dried overnight at 120 °C under vacuum. Approximately 30 mg of the mixture was pressed into a pellet with a diameter of 8 mm and electrochemically lithiated in a three-electrode Swagelok cell with lithium metal counter and reference electrodes and a glass fiber separator (Whatman). After reaching the desired voltage, the cells were opened in an argon-filled glovebox, and the pellets were collected and rinsed with DMC. ^{7}Li MAS NMR spectra were recorded on a Bruker Avance 200 MHz spectrometer at a magnetic field of 4.7 T. The samples were rotated at a spinning speed of 60 kHz. An aqueous 1 M LiCl solution was used as a reference (0 ppm). ^{57}Fe Mössbauer spectroscopic measurements were performed in the transmission mode at room temperature using a constant acceleration spectrometer with a ^{57}Co(Rh) source. All isomer shifts (IS) are given relative to that of α-Fe. The powder samples were sealed in polyethylene bags in an argon-filled glovebox to avoid contact with air during the measurement.

2.5. Isothermal Microcalorimetry. Detection of the heat flow under isothermal conditions was performed with a TAM IV microcalorimeter (TA Instruments) comprising a custom-made sample holder for coin cells. The cells were connected with Cu−P−bronze wires (36 AWG, Lakeshore) to a VSP multichannel potentiostat (BioLogic, France). The presented data was acquired after internal calibration at a thermostat temperature of 40 °C unless otherwise stated. The uncertainty of the setup was less than ±300 nW. Galvanostatic cycling was conducted in the voltage-limited mode between 3.0 and 0.01 V. The GITT-type experiments (GITT = galvanostatic intermittent titration technique) consisted of 30 min current pulses at 100 mA g ^{1} constant current (CC) rate with 15 h rest time in the discharge and 8 h rest time in the charge step after each current pulse. Due to the current interruption, the heat flow could only be determined as the mean heat flow of the respective current pulse. The mean heat flow was calculated from the integral of the heat flow pulse divided by the length of the respective current pulse (see also Figure S1) using the following equation

$$\dot{Q}_{\mathrm{tot,GITT}}(t) = \frac{\int_t^{t+\Delta t} \dot{Q}_{\mathrm{tot}}\, \mathrm{d}t}{1800\ \mathrm{s}} \quad (1)$$

with t being the duration of the discharge or charge step, $\dot{Q}_{\mathrm{tot}}$ the measured heat flow, and Δt being approximately 10 h.

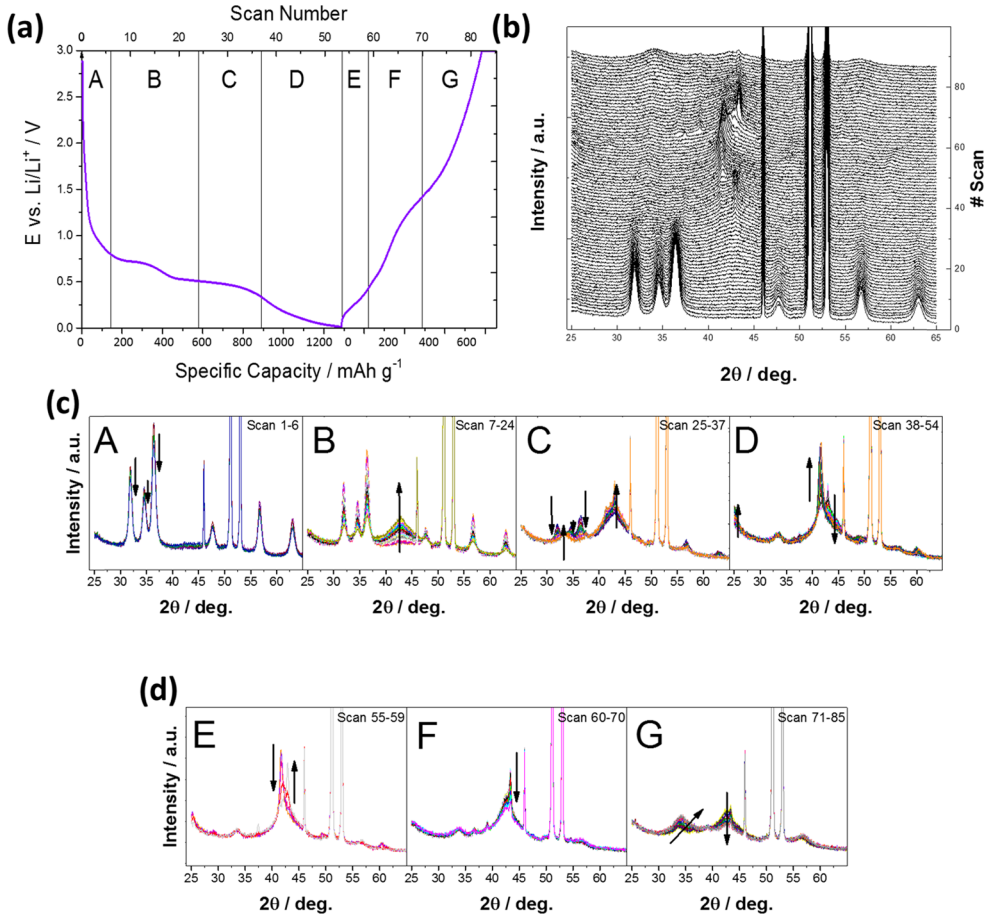

Figure 1. Operando XRD analysis of $Zn_{0.9}Fe_{0.1}O$−C electrodes: (a) Dis-/charge profile for the first de-/lithiation. (b) Waterfall diagram of the XRD patterns obtained during the electrochemical reaction. (c, d) Closeups of these XRD patterns for the different regions highlighted in panel (a) during (c) lithiation and (d) delithiation.

2.6. Entropy and Polarization Measurements. In analogy to the method described by Huie et al.,[34] the overpotential and entropic heat coefficient at different states of charge or discharge were determined from the voltage relaxation steps of a GITT-type experiment. A constant current of 50 mA g^{-1} in intervals of 60 min was applied to the cell that was placed in an incubator (BD 23, Binder), for which the temperature was set to 40 °C. After each current pulse, the voltage was allowed to relax for 40 h, before the temperature was changed. The temperature was varied between 30 and 50 °C in steps of 5 °C and held constant for 1 h at each step, allowing the open-circuit voltage (OCV) to relax (Figure S2). Subsequently, the entropic heat coefficient $\left(\frac{dE_{OCV}}{dT}\right)$ was calculated from the changes of the OCV with respect to the temperature interval as the mean value of six points. The polarization η was estimated from the difference between the initial and final voltage value after 47 h relaxation.

3. RESULTS AND DISCUSSION

3.1. Operando XRD and Ex Situ ^{7}Li NMR and Mössbauer Spectroscopies. To study the phase transitions and structural changes occurring upon electrochemical lithiation and delithiation in carbon-coated $Zn_{0.9}Fe_{0.1}O$ ($Zn_{0.9}Fe_{0.1}O$−C), we performed operando XRD on $Zn_{0.9}Fe_{0.1}O$−C electrodes. For this purpose, the electrode was discharged (lithiated) from OCV to 0.01 V and subsequently charged to 3.0 V with a specific current of 50 mA g^{-1}. The results are shown in Figure 1. Figure 1a depicts the corresponding voltage profile. The waterfall-type plot of the continuously recorded XRD patterns is presented in Figure 1b. Based on the XRD patterns, the lithiation reaction can be divided into four different regions (A, B, C, and D; see also the closeups of the corresponding XRD patterns in Figure 1c). In region A, there is a sloping decrease in voltage until the first plateau at around 0.8 V is reached. In this region, the intensity of the wurtzite-related reflections remains essentially unchanged during the first two scans and gradually decreases afterward. This observation can be explained by the insertion of Li^+ ions into cationic vacancies as reported by Giuli et al.[14] accompanied by the initial reduction of Fe^{3+} to Fe^{2+}. In addition to the decrease of the wurtzite-related reflections, a very careful analysis of the recorded diffractograms reveals a broad signal at about 42.7°, which starts to form in the third scan and has earlier been attributed to the onset of the conversion reaction.[15] In fact, a preliminary evaluation of our recently conducted (operando) X-ray absorption spectroscopy (XAS) study revealed that iron is fully reduced to the metallic state at potentials higher than 0.8 V (accompanied by a partial reduction of zinc), suggesting that in Region A very small metallic iron nanoparticles are formed, which have a size below the detection limit of XRD. As also zinc appears to be partially reduced already at such rather high potentials, we may assume that the initial formation of the iron nanograins kinetically favors the reduction of zinc cations in the vicinity of metallic iron. However, as we observe only one upcoming reflection, it appears reasonable to assign the broad reflection at around

42.7° to an iron/zinc alloy (see also the further discussion), which is in good agreement with the JCPDS reference for $Fe_{13}Zn_{39}$ (JCPDS card file no. 01-072-9761) that has its most intense reflection in this 2θ range. We may note, though, that the precise composition in our case cannot be quantified, and we may accordingly refer to it as $FeZn_x$. Subsequently, in Region B, the wurtzite-related reflections continue to decrease, while the reflection at about 42.7° is gradually increasing, indicating a slight increase of the $FeZn_x$ crystallite size and/or its crystallinity. Starting from scan #35, i.e., in Region C, a new and relatively sharp reflection at 43.0° appeared, which is assigned to the formation of metallic Zn.[15] Simultaneously, the reflections related to the wurtzite structure completely disappeared. Interestingly, the Zn^0 grains are significantly larger (and/or more crystalline) than the $FeZn_x$ nanograins, which might be related to the fact that alloys have a reduced surface energy compared to pure metals, which reduces the driving force of the particles to grow in size. Besides, it appears reasonable to assume that the $FeZn_x$ nanograins are smaller due to the fact that they essentially form around the initially reduced iron dopant, serving as the driving force also for the partial reduction of zinc, thus limiting naturally the potential growth. Differently, the formation of the metallic zinc nanograins is potential-driven and, as a matter of fact, 90% of the comprised metal is zinc. Accordingly, the growth of the zinc nanograins is less limited compared to the growth of the $FeZn_x$ nanograins. In Region D, both reflections (the ones for $FeZn_x$ and Zn^0) disappeared and reflections at 41.0, 48.0, and 60° appeared. This is in excellent agreement with the reported reflections for LiZn (JCPDS card file no. 03-065-3016), i.e., the formation of the lithium zinc alloy, likely comprising also some metallic iron. Interestingly, previous operando XRD investigations of uncoated $Zn_{0.9}Fe_{0.1}O$ showed a shift of the 42.7° reflection toward lower 2θ, rather than the formation of a new reflection.[10] This difference indicates that the presence of the carbon coating kinetically promotes the spontaneous formation of a new phase, presumably as a result of the increased electronic conductivity.

The careful analysis of the diffractograms for the subsequent delithiation (i.e., charge) is presented in Figure 1d. The charge process can be divided into three different regions (E, F, and G). In Region E, the reflections related to LiZn are slightly shifted to larger angles, indicating the depletion of Li in the alloying phase. After scan #55 (i.e., at the end of the first sloping part in the voltage profile), the reflections for both $FeZn_x$ (at 42.8°) and Zn^0 (at 43°) reappear and increase steadily. In Region F, the intensities for both $FeZn_x$ and Zn^0 are simultaneously decreasing. Again, the reflection for metallic Zn^0 disappears first (i.e., at lower potentials). Eventually, the metallic Zn^0 reflection vanished and the reflection for $FeZn_x$ continued decreasing, indicating the oxidation of Fe and Zn. Simultaneously, in Region G, another reflection at 35° is formed, presumably indicating the formation of ZnO with a substantially decreased crystallinity compared to the initial state. Especially, the latter reactions in (F) and (G), however, have to be taken with care. First, it remains to be clarified whether iron and zinc form again some mixed oxides, i.e., whether these two reactions are occurring subsequently or (in part) simultaneously. Second, it will have to be confirmed that the metals are completely reoxidized.

To address especially the latter question, we performed an ex situ ^{7}Li NMR analysis of $Zn_{0.9}Fe_{0.1}O$–C at different states of de-/lithiation. By probing the direct local environment of Li^+ ions, NMR is a highly complementary technique to XRD, which probes the long-range crystal structure. Figure 2a shows

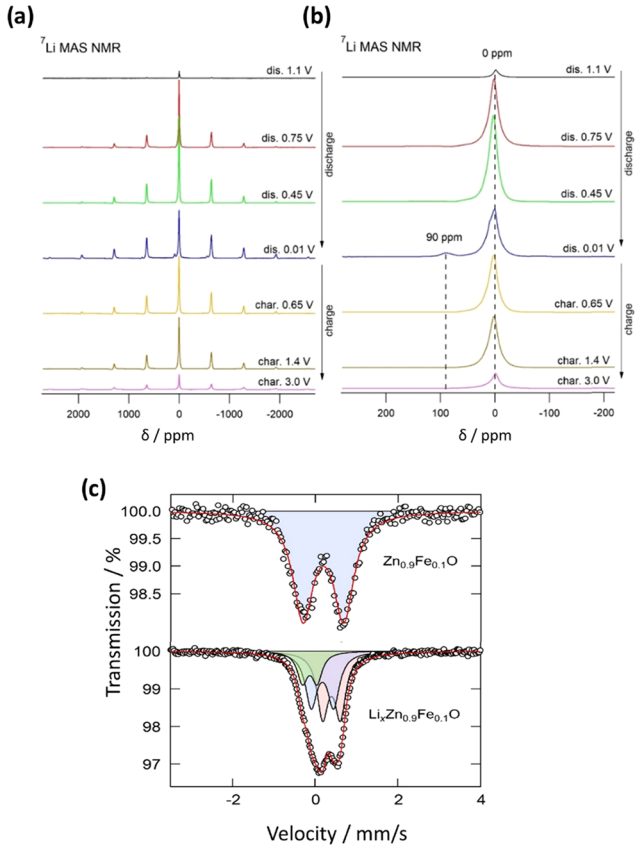

Figure 2. (a) Ex situ ^{7}Li MAS NMR spectra of $Zn_{0.9}Fe_{0.1}O$–C after discharging the sample to 1.1, 0.75, 0.45, and 0.01 V as well as after recharging it to 0.65, 1.4, and 3.0 V. (b) Magnification of the central peak and the evolving peak at 90 ppm and (c) fitted Mössbauer spectra of pristine $Zn_{0.9}Fe_{0.1}O$ (upper panel) and partially lithiated $Zn_{0.9}Fe_{0.1}O$ (discharge cutoff: 0.45 V; the fitting parameters are summarized in Table S1).

the ^{7}Li NMR MAS spectra of $Zn_{0.9}Fe_{0.1}O$–C samples after having been discharged to 1.1, 0.75, 0.45, and 0.01 V as well as for the subsequent charge to 0.65, 1.4, and 3.0 V. All spectra show a peak at 0 ppm, which corresponds to the diamagnetic environment of Li in (diamagnetic) Li_2O as the lithium-containing product for the conversion reaction. The intensity of this peak is increasing upon lithiation and decreasing upon delithiation (see also Figure 2b), indicating the (largely) reversible Li_2O formation during the re-/conversion reaction. It should be noted that at 1.1 V only this one single peak at 0 ppm was present. This is remarkable, as it indicates that there is no intermediate mixed oxide phase, like Li–Fe–O, which would lead to large hyperfine shifts due to a Fermi-contact shift mechanism, prior to the conversion reaction as earlier proposed for $ZnFe_2O_4$.[37] The absence of any additional peak, thus, indicates that the reaction path is different for $Zn_{0.9}Fe_{0.1}O$. As apparent in Figure 2a, all spectra also show a broad spinning sideband pattern, resulting from the presence of (paramagnetic) metallic iron in the sample, even at such rather high potentials of 1.1 V, which is in good agreement with the operando XRD (and XAS) data. In the fully lithiated state at 0.01 V, an additional peak at 90 ppm is observed, which corresponds to the formation of the LiZn alloy formed

at such low potentials.[38] This so-called knight shift often dominates the spectra of metallic samples and is a measure of the density of states at the Fermi level.[39] During the subsequent delithiation, first the peak at 90 ppm disappears and then the intensity of the isotropic peak at 0 ppm is successively decreasing, indicating the backformation of Li_2O. Similarly, also the intensity of the broad spinning sideband pattern is decreasing. However, it does not fully disappear, suggesting that even at the upper anodic cutoff of 3.0 V some iron remains metallic.

To further probe the local magnetic environment of the Fe upon lithiation, we recorded Mössbauer spectra of the pristine sample and after discharging to 0.45 V, i.e., at the end of the second plateau of the voltage profile. The corresponding spectra, along with the least-squares fitting, are shown in Figure 2c. The pristine sample (upper panel) shows only one doublet with an isomer shift (IS) of 0.296 mm s^{-1} and a quadrupole splitting (QS) of 0.98 mm s^{-1}, indicating that all iron is present as Fe^{3+}, since no evidence of a Fe^{2+} signal or ferromagnetic impurities was found, which is in good agreement with a previous XAS study.[40] The large value of the QS is indicating that the ^{57}Fe nuclei are sensing a distorted surrounding. This can be explained by the small crystallite size of the sample (~20 nm), which results in a significant fraction of Fe in the outermost layers of the particle with a more distorted environment,[41,42] especially considering the accompanying cationic vacancies originating from the aliovalent Fe^{3+} doping,[14] as discussed above.

For the Mössbauer spectra of lithiated $Zn_{0.9}Fe_{0.1}O$–C, it was necessary to use three doublets to obtain a reasonable fit of the experimental data, indicating that there are three distinct Fe sites within the particles. Notably, it was not possible to get a reasonable fit with only two doublets, indicated by a large difference between the spectrum and fit, as shown in Figure S3. The three Lorentzian doublets that were used for the fit have an IS of −0.02, 0.28, and 0.50 mm s^{-1} and a QS of 0.35, 0.54, and 0.43 mm s^{-1}, respectively (Figure 2c, bottom panel; fitting parameters are summarized in Table S1). The first site with a slight negative shift, near the zero center, is assigned to γ-Fe^0.[43] The second site with an IS of 0.28 mm s^{-1} is close to reported values for Fe_3Zn_{10} and Fe_5Zn_{21}. The IS of the third site (0.50 mm s^{-1}) does not correspond to the IS of any reported FeZn alloy. However, MacEachern et al.[43] investigated thin-film Fe–Zn alloys by Mössbauer spectroscopy and also found a site with a highly positive IS. By extrapolation of the IS of Fe–Zn alloys as a function of their Fe concentration, they assigned this site to a diluted Fe-in-Zn alloy phase.

Summarizing, our results confirm that iron is reduced to metallic Fe^0, presumably forming some (sub-)nanocrystalline nucleus around which an alloy of Fe and Zn is formed with a decreasing concentration of Fe toward the direction away from the iron nucleus. While this generally confirms

the assignment of the broad XRD reflection at 42.7° to an $FeZn_x$ alloy, the detection of only one phase indicates that there is no distinct phase separation and/or that the crystal structure is very similar for the different Fe concentrations. Based on these complementary results, we, thus, propose the following processes during the first de-/lithiation

$$Zn_{0.9}Fe_{0.1}O + 0.05Li^+ + 0.05e^- \rightarrow Li_{0.05}Zn_{0.9}Fe_{0.1}O \quad (A)$$

$$Li_{0.05}Zn_{0.9}Fe_{0.1}O + (0.25 + 2x)Li^+ + (0.25 + 2x)e^- \rightarrow (0.9 - x)ZnO + yFe^0 + (0.1 - y)FeZn_x + 1/2(0.3 + 2x)Li_2O \quad (A–B)$$

$$(0.9 - x)ZnO + 2(0.9 - x)Li^+ + 2(0.9 - x)e^- \rightarrow (0.9 - x)Zn^0 + (0.9 - x)Li_2O \quad (C)$$

$$(0.9 - x)Zn^0 + (0.1 - y)FeZn_x + (1 - y)Li^+ + (1 - y)e^- \rightarrow (0.9 - x)LiZn + (0.1 - y)Li_xFeZn_x \quad (D)$$

$$(0.9 - x)LiZn + (0.1 - y)Li_xFeZn_x \rightarrow (0.9 - x)Zn^0 + (0.1 - y)FeZn_x + (1 - y)Li^+ + (1 - y)e^- \quad (E)$$

$$(0.9 - x)Zn^0 + (0.9 - x)Li_2O \rightarrow (0.9 - x)ZnO + 2(0.9 - x)Li^+ + 2(0.9 - x)e^- \quad (F)$$

$$(0.1 - y)FeZn_x + xLi_2O \rightarrow (0.1 - y)Fe^0 + x(0.1 - y)ZnO + 2 \times (0.1 - y)Li^+ + 2 \times (0.1 - y)e^- \quad (F–G)$$

$$0.1Fe^0 + 0.1Li_2O \rightarrow 0.1FeO + 0.2Li^+ + 0.2e^- \quad (G)$$

Note that especially the last step is not complete, i.e., not all iron is reoxidized, as indicated by the ex situ ^7Li NMR analysis. Moreover, it remains unclear whether the two metal oxides are formed separately or whether there are some mixed oxides formed upon charge. Also, it was assumed for clarity reasons that the $FeZn_x$ alloy is alloying with lithium with a ratio between Zn and Li of one to one, similar to the pure LiZn alloy.

3.2. Isothermal Microcalorimetry: 1st Cycle. Following the investigation of the reaction mechanism and the given electrochemical reaction of iron-doped zinc oxide and lithium, the corresponding changes in enthalpy (ΔH_R^0) can be estimated based on literature values (Table S2). Due to the lack of available standard formation enthalpies of $Zn_{0.9}Fe_{0.1}O$–C, we used the value for ZnO instead, since the deviation should be reasonably small for our purpose. In an ideal galvanic cell, the electrical work (W_{el}) is equal to the change in the enthalpy of reaction. Nevertheless, in real devices also inherent heat losses lowering the overall energy efficiency have to be taken into account. Given the isochoric conditions in sealed coin cells, the first law of thermodynamics can be written as

$$\Delta U = \Delta H_{tot} = Q_{tot} - W_{el} \quad (2)$$

with the internal energy U, the total enthalpy change ΔH_{tot}, and Q_{tot} as the overall heat being released or absorbed by the cell. Isothermal microcalorimetry measures the heat flow $\dot{Q} = \frac{dQ}{dt}$ (also denoted q) during operation and, therefore, allows for the determination of Q_{tot}. The electrical work (W_{el}) can be calculated by integrating the cell voltage with respect to the capacity obtained. In Table S3, theoretical and experimentally determined values for the changes in enthalpy are summarized. Regarding the initial lithiation of $Zn_{0.9}Fe_{0.1}O$,

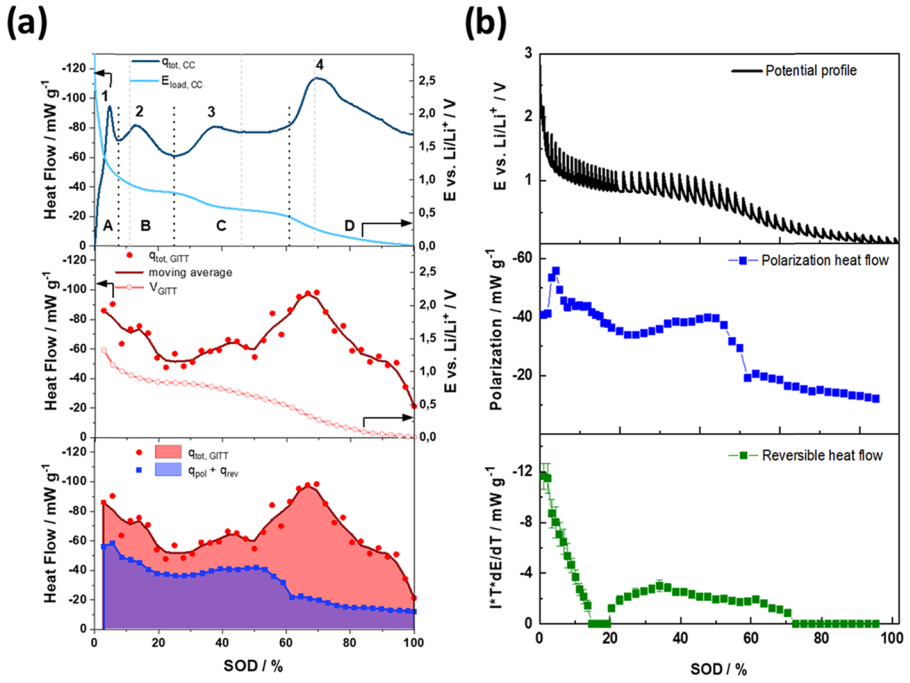

Figure 3. (a) Top: Voltage and heat flow profile for the first lithiation of a $Zn_{0.9}Fe_{0.1}O$−C half-cell at a constant current of 100 mA g^{-1} with a cutoff voltage of 0.01 V; middle: mean total heat flow of the first lithiation measured in the GITT-type experiment (100 mA g^{-1}, 15 h relaxation), moving average of the mean heat flow, and the voltage under load before relaxation; bottom: mean total heat flow compared with the sum of the polarization heat flow and the reversible heat flow; (b) from top to bottom: voltage profile for the GITT experiment (in black), the estimated heat originating from polarization (in blue), and the entropic heat (in green) during the first lithiation of $Zn_{0.9}Fe_{0.1}O$−C.

the theoretical change in enthalpy ΔH_R^0 was calculated to be about −3300 J g^{-1}, whereas the measured total enthalpy ΔH_{tot} is −7386 J g^{-1}. Neglecting the typically small contributions of entropic changes, the comparison of the theoretically calculated and experimentally determined values for the resulting enthalpy changes and specific capacities reveals a large discrepancy. Therefore, additional reactions have to be considered that explain the surplus in heat. For the first lithiation, electrolyte decomposition and SEI formation certainly have to be taken into account. The general energy balance model for batteries, developed by Bernardi et al.,[44] describes the total enthalpy ΔH_{tot} as a sum of contributions from the enthalpy of reaction, the enthalpy of mixing, phase changes, and changes in heat capacity. However, as in most thermal characterization studies on batteries, the enthalpy of mixing and phase changes are considered negligible and heat capacities are nearly constant under isothermal conditions. Thus, we utilized the simplified form of the energy balance model as described by Downie et al.[30]

$$\dot{Q}_{tot} = |I(E_{load} - E_{OCV})| + IT\left(\frac{dE_{OCV}}{dT}\right) + \dot{Q}_{par} \quad (3)$$

The model includes three main contributions to the measured total heat flow $\dot{Q}_{tot}$: heat flow from polarization, entropic changes, and heat flow due to side reactions. The first term $I(E_{load} - E_{OCV})$ describes polarization heat flow ($\dot{Q}_{pol}$) arising from Ohmic losses, charge transfer overpotentials, and mass transfer limitations. The values for E_{load} and E_{OCV} were determined as the initial and final OCVs of the voltage relaxation steps during the GITT measurements (see also Figure S2a). Entropic heat flow $\dot{Q}_{rev} = IT\left(\frac{dE_{OCV}}{dT}\right)$ originates from changes in entropy due to the Faradaic reaction. The entropic heat coefficient $\left(\frac{dE_{OCV}}{dT}\right)$ was determined potentiometrically by the offset of the OCV due to a defined change in temperature (Figure S2b). All other contributions to the heat flow from non-Faradaic reactions, i.e., parasitic reactions, are summed up in the last term $\dot{Q}_{par}$.

3.2.1. 1st Discharge (Lithiation). In Figure 3a, the recorded heat flow and corresponding voltage profile of the first discharge are depicted. The negative heat flow values indicate the direction of the heat flow from the cell to the heat sink of the calorimeter. Four pronounced peaks at 5, 13, 38, and 70% state of discharge (SOD) as well as a shoulder at 1.5% SOD (Figure S4) characterize the heat flow of the first lithiation. The heat flow profile is reproducible and characteristic for the first lithiation, even at lower currents (Figure S5). Comparing the heat flow profile with the operando XRD data, the following assignment of the heat flow peaks to the Regions (A)−(D) can be made. The shoulder and peak 1 in Region A are assigned to the initial Li^+ insertion and the onset of the formation of small iron nanograins, respectively. Peak 2 in Region B (i.e., the first plateau in the voltage profile) is assigned to the crystallization and growth of the $FeZn_x$ nanograins, accompanied by the reduction of the initial oxide. Peak 3 is assigned to the Zn^0 formation in Region C (i.e., the second plateau in the voltage profile), and peak 4 corresponds to Region D, i.e., the formation of the lithium alloys. The occurrence of a peak in the heat profile at the formation of every new phase can be explained by the required surface energy related to the different reactions, especially the nucleation step. Since the creation of a large interface requires energy (due to surface tension), the formation of each new phase requires an overpotential to balance this extra energy. However, the nucleation is followed by the growth of these new phases. Thereby, the relative interfacial area is decreasing

and the additional energy is released as heat. Interestingly, the position of the peaks in the heat flow suggests a much earlier nucleation of new phases compared to the operando XRD data. This can be explained, first, by the slightly higher temperature of 40 °C, i.e., faster kinetics, while the XRD experiment was conducted at room temperature, and, second, by the fact, that crystallites of the new phase need to have a certain minimum size to be detectable by XRD, whereas the heat release should occur right after the nucleation. Obviously, the transition from conversion (Region C) to pure alloying reactions (Region D), identified by operando XRD, is accompanied by a large heat release (peak 4). In summary, we made consistent observations with the subdivision by operando XRD on the one hand and with the general shape of the voltage profile on the other hand. However, the origin of the individual features in the heat flow profile can only be identified after deconvolution of the total heat flow into the different contributions.

3.2.2. Separation of Heat Flow Sources: 1st Discharge. To determine the different contributions to the heat flow, i.e., every single term in eq 3, at different states of discharge (lithiation), we designed a set of experiments to measure the OCV under thermodynamic equilibrium conditions. For resolving the first term in eq 3, the heat flow from polarization ($\dot{Q}_{pol}$) was estimated from multiplying the overpotential $\eta = E_{load} - E_{OCV}$ with the specific current. The entropic heat coefficient $\left(\frac{dE_{OCV}}{dT}\right)$ of the second term was derived by measuring the change of the OCV with respect to the temperature interval. Similar to the method described by Huie et al.,[34] a GITT-type experiment in combination with a temperature variation during the OCV step was conducted to determine both the overpotential and the entropic heat coefficient in one experiment. Due to the intermittent current technique, the total heat flow $\dot{Q}_{tot}$ had to be calculated as the mean value of the heat flow over the respective time interval, denoted $\dot{Q}_{tot,GITT}$. The total heat flow $\dot{Q}_{tot,GITT}$ and the corresponding voltage profile of the GITT-type experiment are depicted in Figure 3a together with the heat flow and voltage profile of the constant current (CC) measurement described in the previous section. Due to the relatively long time intervals chosen, the first two peaks in the heat flow curve of the constant current experiment are hardly resolved in the GITT-type experiment. Remarkably, the local maximum in heat flow at 38% SOD (peak 3) vanishes in the GITT-type experiment or shifts to a significantly higher SOD. At the same time, the voltage curve in Region B does not follow two plateaus as during the constant current measurement but forms a long sloping region, though with a change in slope at around 40% SOD. This observation indicates that the position of the third peak, which is assigned to the formation of Zn^0, and the distinct separation of the two voltage plateaus originate from kinetic limitations. As discussed earlier, Fe starts to be reduced at higher potentials than Zn and may kinetically favor the formation of the new $FeZn_x$ phase. Once all of the Zn^{2+} in the direct vicinity of those sites is reduced, the Zn^{2+} diffusion becomes the limiting step for the growth of the $FeZn_x$ phase. Consequently, a new Zn^0 phase is formed (earlier) during constant current lithiation. However, during the long OCV relaxation steps, the Zn^{2+} diffusion appears to be at least less limiting and the growth of the $FeZn_x$ phase is prolonged.

The polarization heat flow $\dot{Q}_{pol}$ was estimated from the potential difference between the initial voltage under load and the final OCV in the GITT-type voltage relaxation experiments at different states of discharge (Figure 3b). Although the relaxation time was 47 h, the OCV does not reach a constant value but a quasistable state with a small slope (Figure S2a). It has been reported that the determination of the equilibrium potential for conversion materials would be difficult with GITT-type experiments due to their intrinsic hysteresis and extraordinarily long voltage relaxation times.[45] Since we were not able to determine the full polarization of our system in a reasonable time, the polarization heat flow was underestimated, too. The following discussion of the different contributions to the total heat flow will therefore be kept qualitatively. The polarization heat flow $\dot{Q}_{pol}$ forms a sharp peak at the beginning of the first discharge and levels off until a minimum is reached at 25% SOD (Figure 3b). The weak, but constant increase until 55% SOD is followed by an abrupt decrease. From 60% until 100% SOD, the polarization heat flow remains low and decreases constantly further. The sharp peak at the beginning matches the initial peak for the measured heat flow (A), which was assigned to the formation of metallic Fe^0. The minimum at 25% SOD also nicely resembles the minimum observed in the measured heat flow, which correlates with the alloying of iron and zinc. Referring to the operando XRD results, the abrupt change in polarization coincides with the termination of the conversion reaction. Accordingly, the conversion contribution is connected to much larger polarization heat flow than the contribution from alloying.

The reversible heat flow was derived from the changes in cell voltage upon temperature change during the quasistable state of the voltage relaxation steps at different SODs. The temperature was varied between 30 and 50 °C in 5 °C intervals, and the voltage was allowed to relax for 1 h. Subsequently, the entropic heat coefficient $\left(\frac{dE_{OCV}}{dT}\right)$ was calculated from the difference between the initial and end value of the relaxation step with respect to the temperature interval (Figure 3b).

The reversible heat flow due to entropic changes in the system is large at the beginning and decreases constantly, reaching the detection limit at 17% SOD. It starts to rise again at 20% SOD, reaching a maximum at about 35% SOD and decreases afterward until it reaches the detection limit at 75% SOD. In terms of entropy, an initial increase is observed, which is attributed to the loss of crystallinity of the initial $Zn_{0.9}Fe_{0.1}O-C$ particles. In fact, this behavior was observed exclusively during the first lithiation. The following decrease in entropy with a maximum in Region C is connected to the formation and growth of $FeZn_x$ and elemental Zn^0 nanograins. It can be concluded that changes in entropy and, thus, the reversible heat flow are more pronounced in the regions where conversion reactions are the dominant Faradaic process. Noteworthy, in conventional lithium insertion materials, $\dot{Q}_{rev}$ and $\dot{Q}_{pol}$ show typically values of the same order of magnitude at dis-/charge rates of C/10.[26] However, in the case of $Zn_{0.9}Fe_{0.1}O-C$, $\dot{Q}_{pol}$ exceeds $\dot{Q}_{rev}$ by a factor of 10. Hence, the contribution of the reversible heat flow is almost negligible in the case of $Zn_{0.9}Fe_{0.1}O-C$ and the polarization heat flow mostly dictates the course of the total heat flow.

Regarding the energy balance model in eq 3, the parasitic heat flow $\dot{Q}_{par}$ can be calculated as the difference between the measured total heat flow $\dot{Q}_{tot}$ and the sum of $\dot{Q}_{pol}$ and $\dot{Q}_{rev}$. Since $\dot{Q}_{pol}$ remains underestimated, the derived values for the parasitic heat flow can only be a rough estimate, oversized by

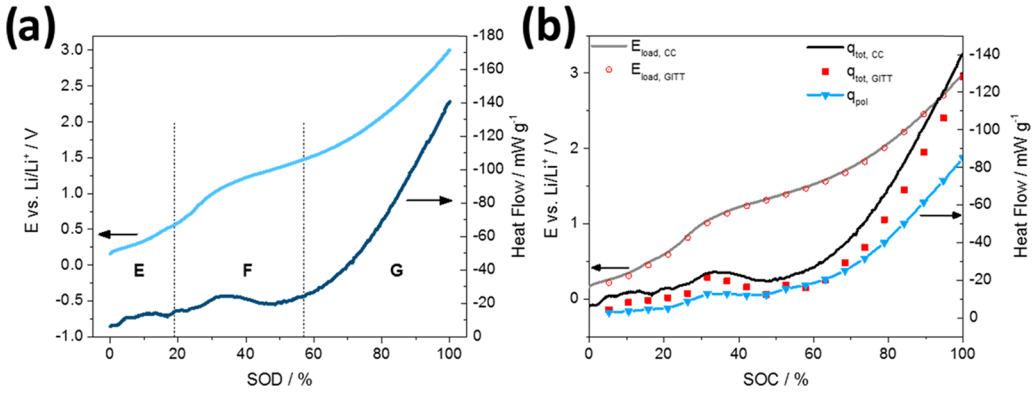

Figure 4. (a) Voltage profile (in light blue) and heat flow (in dark blue) for the first delithiation (i.e., charge) of a $Zn_{0.9}Fe_{0.1}O$−C half-cell (specific current: 100 mA g^{-1}; cutoff potentials: 0.01 and 3.0 V). (b) Comparison of the heat flow under constant current (CC; the solid black line), the heat flow during the GITT-type measurement (red squares), and the estimated heat originating from polarization (the solid light-blue line with triangles) for the first delithiation; the corresponding voltage profile for the CC (the solid gray line) and GITT (hollow red spheres) experiment are provided as well.

trend. The resulting course of the parasitic heat flow together with the sum $\dot{Q}_{pol} + \dot{Q}_{rev}$ and the total heat flow are depicted in Figure 3a (bottom panel). In the first half of the lithiation, the sum $\dot{Q}_{pol} + \dot{Q}_{rev}$ resembles essentially the course of the total heat flow. In the second half of the lithiation process, the parasitic heat flow becomes the major heat source with a maximum at 70% SOD. Heat flow measurements at different temperatures are supporting our assignment (Figure S6). With an increased temperature, the heat flow in Region D increases, as expected for parasitic reactions, while polarization diminishes and entropic changes are small anyways. According to the operando XRD data, the sharp increase in parasitic heat flow coincides with the termination of the conversion reaction. The observed large parasitic heat flow is therefore related to the voltage region in which the alloying reaction occurs. Generally, though, parasitic heat flow is caused by irreversible electrolyte reactions, i.e., its reductive decomposition and the formation of the SEI.[46] Considering the large volume variation that accompanies the formation of the alloy,[47] we attribute the large parasitic heat flow in Region D to an increased electrolyte decomposition and SEI formation on the freshly formed surface of the alloy grains, which are continuously expanding with an increasing lithium content.

3.2.3. 1st Charge (Delithiation). In accordance with the asymmetry of the charge and discharge voltage profiles, the shape of the heat flow profile during the 1st delithiation of $Zn_{0.9}Fe_{0.1}O$−C (Figure 4a) is asymmetric to the 1st lithiation heat flow profile. In contrast to the constantly rather large heat flow during lithiation, the delithiation heat flow is much lower in the first half of the charge process. In Region E, below 25% state of charge (SOC), a constant but faintly increasing heat flow was observed, followed by a broad peak between 25 and 55% SOC in Region F. At 55% SOC, however, the heat flow experiences a steep and continuous increase (Region G). The division of the charge process into three different regions (E, F, and G) is in accordance with the operando XRD results, and the transitions between the regions coincide with the inflections in the corresponding voltage profile as well. Therefore, in Region E, the dealloying of LiZn, resulting in the formation of Zn^0, is accompanied by a small heat flow, whereas the reconversion of Zn^0 and the simultaneous dealloying of $FeZn_x$ in Region F are characterized by an initially enhanced increase in heat flow that turns into a decay reaching the region limit. Finally, in Region G, the ongoing reconversion is accompanied by a steep and continuous increase in heat flow until the current was cut off at 3.0 V.

3.2.4. Separation of Heat Flow Sources: 1st Charge. In analogy to the separation approach for the lithiation step, $\dot{Q}_{pol}$ and $\dot{Q}_{rev}$ were determined potentiometrically and then compared with the total heat flow measured during a GITT-type experiment (Figure 4b). The first remarkable observation is that unlike the lithiation case, the shapes of the charge and heat profile recorded during the GITT experiment resemble very well the shape of the respective profiles from constant current measurements. Generally, the reversible heat flow is negligible throughout the charge process, whereas the polarization heat largely resembles the evolution of $\dot{Q}_{tot}$. Above 80% SOC, though, $\dot{Q}_{pol}$ deviates significantly from $\dot{Q}_{tot}$, indicating an increase in parasitic heat at elevated potentials along with the completion of the conversion reaction, which we assign to the oxidation of the previously formed SEI, also referred to as "quasireversible SEI formation".[48−52]

Let us briefly summarize the findings of the investigations of the first de-/lithiation cycle of $Zn_{0.9}Fe_{0.1}O$−C by isothermal microcalorimetry: We found that the heat flow profiles for the lithiation and delithiation reaction exhibit a different shape, i.e., are not symmetric. This indicates that the reaction pathways during charge and discharge are different. The changes in heat flow coincide with inflections in the voltage profile and the phase changes observed by operando XRD. Therefore, IMC proved to be capable of differentiating the single reaction steps in the first de-/lithiation cycle of $Zn_{0.9}Fe_{0.1}O$−C. We learned from the differences in heat flow obtained at constant current conditions and conditions approaching the equilibrium state that kinetic limitations can cause characteristic features in the heat flow profile. Furthermore, the separation of the different contributions to the total heat flow revealed that the shape of the overall heat flow profile is determined by changes in polarization and parasitic reactions in the system. During lithiation, a large polarization heat flow was observed in those regions where the conversion reaction dominates, while an increased parasitic heat flow was observed in the regions where majorly the alloying reaction occurs, since the accompanying volume expansion triggers a continuous electrolyte decomposition. The delithiation appears less kinetically controlled, presumably due to the very small size and (sub-)-

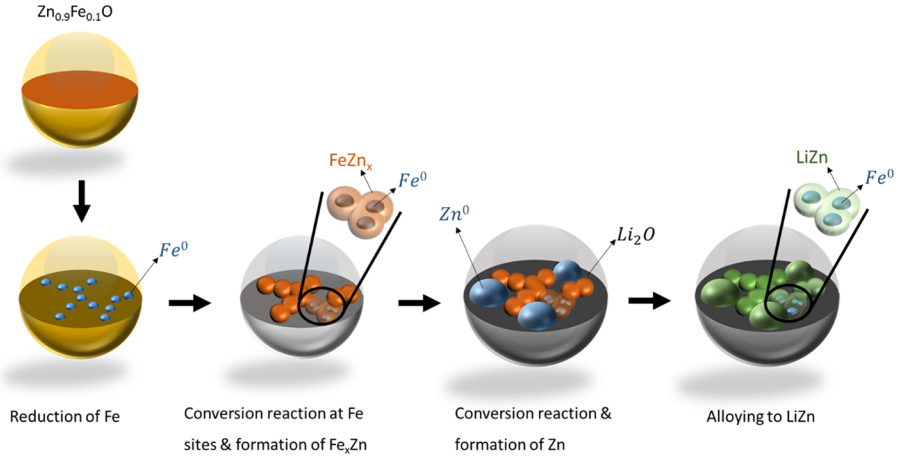

Figure 5. Schematic illustration of the initial lithiation mechanism according to the herein proposed nucleation site model under nonequilibrium conditions. For clarity reasons, the alloying reaction of $FeZn_x$ and Li is not specifically indicated.

nanocrystalline nature of the previously formed nanograins. Nevertheless, this does not prevent a high polarization upon charge for the reconversion, which is assigned to the relatively poor electronic conductivity within the electrode as a result of the essentially insulating nature of the metal oxides formed.[53] Moreover, at potentials above 1.5 V, an increased parasitic heat flow was observed, indicating the oxidation of the SEI.

3.3. General Reaction Mechanism. Based on the sum of the results obtained by operando XRD and ex situ ^{7}Li NMR and Mössbauer spectroscopies, as well as isothermal microcalorimetry (IMC), we propose a refined mechanism for the initial lithiation of (carbon-coated) iron-doped zinc oxide following a "nucleation site model", as schematized in Figure 5. The initial lithium cation insertion and subsequent further reduction of iron, indicated by operando XRD, ex situ ^{7}Li NMR (i.e., the broad sideband pattern already at 1.1 V), and the first IMC peak, appear to play an essential role for the overall lithiation reaction. In fact, the network of ultrafine metallic iron nanograins serves as the initial nucleation site for the reduction of zinc and the subsequent alloying of metallic zinc with iron by ensuring the required electron flow within the original nanoparticles. This kinetically favored reduction of the intimately neighbored zinc cations is reflected by the slightly higher first voltage plateau in the discharge profile. At about 30% SOD, the discharge profile shows a second plateau at a slightly lower potential, which is accompanied by the third peak in the heat profile. Simultaneously, the operando XRD data reveals the formation of relatively large secondary Zn^0 particles. We may explain this as follows: The Fe^0 nucleation sites kinetically favor the conversion reaction in their immediate vicinity, but the reduction of relatively farther zinc cations is kinetically hampered. As the diffusion of zinc becomes the limiting step for the growth of the $FeZn_x$ phase, the potential is decreasing and Zn^{2+} is reduced to elemental Zn^0. Noteworthy, the two plateaus tend to merge when approaching equilibrium conditions for the lithiation reaction, as observed for the GITT experiment or when sufficiently slowing down the discharge rate to C/200 (Figure S7), thus overcoming (or at least reducing) the charge and mass transport limitations. Eventually, the metallic zinc (and the zinc comprised in the alloy with iron) further alloys with lithium in the low-potential region, accompanied by an ongoing electrolyte decomposition as a result of the corresponding volume expansion.

For the subsequent delithiation, no severe kinetic limitations occur, as the whole system, composed of metallic iron and LiZn alloy, is highly conductive. Accordingly, the overall shapes of the charge profile and heat flow evolution do not significantly differ under GITT conditions compared to the constant current charge. Nevertheless, a large contribution of polarization to the heat flow due to the rather insulating nature of the metal oxides formed upon reconversion and, particularly, the extensive parasitic heat flow at very high potentials as a result of the partial SEI decomposition highlight the limited use of charging conversion-type materials to elevated cutoffs like 3.0 V in real devices (in addition to the accompanying loss in the energy density for the resulting full cell[54]).

3.4. Isothermal Microcalorimetry: Subsequent Cycles. Following the finding that the first cycle is characterized by large contributions from parasitic heat flow due to SEI formation, which may obscure further features in the heat flow profile, we studied also selected subsequent cycles to gain a complete picture of the de-/lithiation mechanism of $Zn_{0.9}Fe_{0.1}O$−C and the potential of isothermal microcalorimetry in characterizing CAMs.

3.4.1. Discharge (Lithiation) Process. We chose exemplarily the 24th cycle, as the discharge/charge capacity had well stabilized after about 20 cycles, including a highly reversible shape of the corresponding voltage profiles, as shown for the previous 23 cycles in Figure S8. Similarly, the heat flow profiles reveal an essentially identical shape, as depicted for the cycles 24−26 in Figure S9. It appears noteworthy that the total heat generated throughout the representative 24th lithiation is only about one-third compared to that of the 1st cycle (Table 1). Regarding the discharge voltage profile, the two characteristic plateaus of the first lithiation merge into one continuously sloping curve (see Figure 6a; in line with previous results[15]). Meanwhile, the corresponding heat flow profile exhibits less pronounced, yet distinguishable features. The three inflections at 7.5, 46, and 69% SOD are correlated to different lithiation processes, indicating that the occurring electrochemical reactions are similar to those of the first lithiation (though there is apparently no initial insertion anymore). Generally, compared to the heat flow during the first lithiation, the transitions from Region B to Region C and from Region C to Region D are shifted toward higher SODs, presumably due to the lack of capacity originating from parasitic reactions (see

Table 1. Summary of the Specific Capacities and Dissipated Heat for the 1st and 24th Cycle at Different States of Dis-/Charge[a]

cell	cycle	cutoff potential (V)	step	capacity (mAh g^{-1})	heat (J mg^{-1})	heat (J A^{-1} h^{-1})
#1	1st	3.0	discharge	1550	4.5	2896
			charge	990	1.4	1383
#1	24th	3.0	discharge	1002	1.7	1688
			charge	947	1.5	1582
#2	24th	2.0	discharge	647	0.77	1190
			charge	629	0.39	625
#3	24th	1.5	discharge	498	0.53	1062
			charge	475	0.19	399

[a]For a better comparability, the evolved heat is given in two different relations, i.e., with respect to the mass of active material and with respect to the capacity at the given state of dis-/charge.

also Table 1). The heat flow peak in Region A is attributed to the reduction of Fe^{2+}. Notably, the direct comparison with the first lithiation shows the dimension of the heat flow due to initial polarization (Figure 6a). In Region B, the formation of the $FeZn_x$ alloy and the accompanying conversion is characterized by an ascending slope of the heat flow. After a small drop, a constant heat flow attends the formation of elemental Zn in Region C, indicating the completion of the conversion reaction. The alloying of Zn with Li takes place in Region D, where the heat flow describes a little "valley" with a local minimum at around 80% SOD.

Following the same approach as for the heat flow analysis of the first cycle, we tried to separate the different contributions. However, when calculating the values for the polarization heat and the entropic changes, it becomes clear that their share does not account for the majority of the measured heat flow (Figure 6b). Instead, parasitic heat appears to largely contribute to the measured heat flow $\dot{Q}_{tot}$. The contribution of the polarization heat experiences a sharp decline at the end of Region B (50% SOD). Since the heat flow originating from entropic changes plays only a minor role also for the 24th discharge, parasitic heat flow becomes the major heat source beyond 50% SOD, according to the applied energy balance model. This indicates that the electrolyte decomposition continues in subsequent cycles with a constant amount.

3.4.2. Charge (Delithiation) Process. Comparing the delithiation voltage and heat flow profiles for the 1st and 24th cycle (Figure 6c) reveals that the shape is essentially maintained. Thus, the underlying electrochemical processes can be considered to be identical. This supports, in turn, the previous statement that the lithiation is following essentially the same reaction pathway in subsequent cycles. Furthermore, the separation of the heat flow contributions shows that the polarization heat evolution follows basically the same trend as the overall heat flow profile and provides the major contribution at low potentials, i.e., up to a SOC of 80%. At elevated potentials, however, the polarization heat flow levels off, while the overall heat keeps increasing steeply (Figure 6d). This behavior is slightly different from the first delithiation and indicates that the parasitic heat flow at such elevated potentials is relatively more pronounced in subsequent cycles. As a matter of fact, increasing capacity values with prolonged cycling are frequently reported for conversion(/alloying)-type materials, indicating an increased SEI formation and its (partial) oxidation upon charge at elevated potentials.[48−52]

3.4.3. Suppression of Parasitic Heat. To diminish the parasitic heat flow during cycling, we decreased the anodic cutoff voltage for the charge process. In fact, lowering the upper cutoff voltage is expected to suppress the SEI oxidation and thereby the parasitic heat flow at low potentials during lithiation. To remain consistent with the previous results, we investigated two more cells with anodic cutoff voltages of 1.5 and 2.0 V for 24 cycles. Thereby, the overall heat released in the 24th cycle decreases dramatically with the stepwise reduction of the anodic cutoff voltage, especially upon charge (Table 1). To account for the reduced capacity due to the reduced anodic cutoff voltage, we will discuss the changes in the evolved heat with respect to the respective capacity. In the discharge step, the heat is reduced by 25% (3.0 V: 1688 J A^{-1} h^{-1} vs 2.0 V: 1190 J A^{-1} h^{-1}) and 31% (3.0 V: 1688 J A^{-1} h^{-1} vs 1.5 V: 1062 J A^{-1} h^{-1}). During charge, the overall heat with respect to capacity decreases even more drastically by 60% (3.0 V: 1582 J A^{-1} h^{-1} vs 2.0 V: 625 J A^{-1} h^{-1}) and 75% (3.0 V: 1582 J A^{-1} h^{-1} vs 1.5 V: 399 J A^{-1} h^{-1}). The different impact on lithiation and delithiation is also observed in the corresponding heat flow and voltage profiles (Figure 6e,f). The heat of the charge step is much more affected, since Region G in the heat flow profile with large contributions from parasitic and polarization heat flows is simply omitted. However, the heat in the discharge step is also significantly reduced, particularly at low potentials where parasitic heat flow was identified to be the main contribution. The effect of the reduction of the anodic cutoff voltage is further emphasized by plotting the heat flow against the cell voltage (Figure S10). The peak in heat flow at about 1.25 V, attributed to the reduction of Fe, is diminished at lower anodic cutoff voltages. More importantly, below 0.5 V, the heat flow is also reduced, indicating a successful suppression of the parasitic heat flow in the low-voltage region. Thus, we can conclude that the heat was effectively reduced when applying a lower anodic cutoff voltage and that this effect is not the result of the reduced capacity only. In fact, avoiding specific voltage regions, i.e., electrochemical reactions, with large contributions from polarization heat flow and reducing the parasitic heat flow, ascribed to the inhibition of the continuous electrolyte reduction and SEI oxidation, account for the reduction of the total evolved heat.

4. CONCLUSIONS

This study shows that the combination of XRD, NMR and Mössbauer spectroscopies, and IMC as highly complementary methods allows for a better understanding of the de-/lithiation mechanism of CAMs like $Zn_{0.9}Fe_{0.1}O-C$. As a result, we propose a new nucleation site model for the first lithiation of $Zn_{0.9}Fe_{0.1}O(-C)$. The initially formed metallic iron (sub-)nanograins serve as nuclei for the reduction of zinc cations in their immediate vicinity, leading to the formation of a $FeZn_x$ alloy with decreasing Fe concentrations along with an increasing distance from these nuclei. Subsequently, relatively larger zinc crystals are formed, though the onset of their formation is governed by mass and charge transport limitations, i.e., kinetically driven. While the general reaction mechanism does not change upon continuous cycling, as revealed by IMC (apart from the initial Li^+ insertion into cationic vacancies), the careful IMC analysis also indicates that the oxidation of the SEI at elevated charge potentials is increasing with cycling and largely contributing to the total heat evolving. Limiting the delithiation potential to 2.0 V or

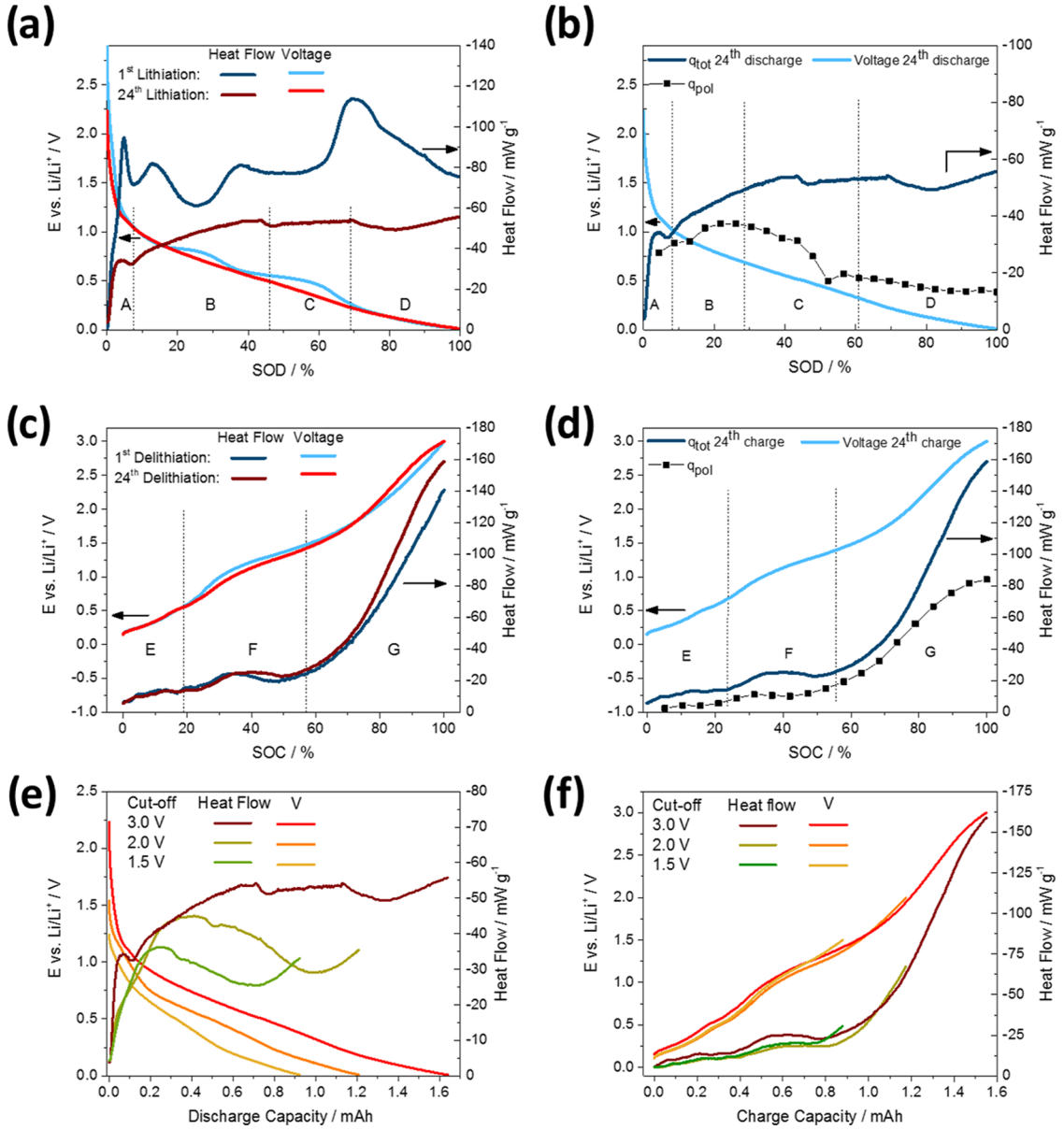

Figure 6. (a) Heat flow and voltage profiles for the 1st and 24th lithiation for galvanostatically cycled $Zn_{0.9}Fe_{0.1}O$–C half-cells at a specific current of 100 mA g^{-1} and a temperature of 40 °C. (b) Comparison of the heat flow under constant current (the dark blue line) and the estimated heat originating from polarization (the solid black line with squares) for the 24th lithiation. (c) Heat flow and voltage profiles for the 1st and 24th delithiation. (d) Comparison of the heat flow under constant current (the dark blue line) and the estimated heat originating from polarization (the solid black line with squares) for the 24th delithiation. (e) Lithiation and (f) delithiation heat flow and voltage profiles for the 24th cycle with different anodic cutoff potentials (1.5, 2.0, and 3.0 V) at a specific current of 100 mA g^{-1} and a temperature of 40 °C.

even 1.5 V successfully addresses this issue, as confirmed by a substantially reduced heat evolution relative to the capacity obtained for the delithiation and lithiation, which provides valuable insights for the further development of CAMs in particular and conversion- as well as alloying-type materials in general.

AUTHOR INFORMATION

Corresponding Authors

Alexander Hoefling − *Helmholtz Institute Ulm (HIU), 89081 Ulm, Germany; Karlsruhe Institute of Technology (KIT), 76021 Karlsruhe, Germany*; Email: alexander.hoefling@kit.edu

Dominic Bresser − *Helmholtz Institute Ulm (HIU), 89081 Ulm, Germany; Karlsruhe Institute of Technology (KIT), 76021 Karlsruhe, Germany*; orcid.org/0000-0001-6429-6048; Email: dominic.bresser@kit.edu

Authors

Jakob Asenbauer − *Helmholtz Institute Ulm (HIU), 89081 Ulm, Germany; Karlsruhe Institute of Technology (KIT), 76021 Karlsruhe, Germany*

Sylvio Indris − *Helmholtz Institute Ulm (HIU), 89081 Ulm, Germany; Institute for Applied Materials, Karlsruhe Institute of Technology, 76344 Eggenstein-Leopoldshafen, Germany;* orcid.org/0000-0002-5100-113X

Jens Tübke − *Helmholtz Institute Ulm (HIU), 89081 Ulm, Germany; Karlsruhe Institute of Technology (KIT), 76021 Karlsruhe, Germany; Applied Electrochemistry, Fraunhofer-Institute for Chemical Technology, 76327 Pfinztal, Germany*

Stefano Passerini − *Helmholtz Institute Ulm (HIU), 89081 Ulm, Germany; Karlsruhe Institute of Technology (KIT), 76021 Karlsruhe, Germany;* orcid.org/0000-0002-6606-5304

Author Contributions

⊥J.A. and A.H. contributed equally to this study.

Notes

The authors declare no competing financial interest.

ACKNOWLEDGMENTS

The authors would like to acknowledge financial support from the Vector foundation within the NEW E^2 project and the Helmholtz Association. This work contributes to the research performed at CELEST (Center for Electrochemical Energy Storage Ulm-Karlsruhe).

REFERENCES

(1) Scrosati, B.; Garche, J. Lithium Batteries: Status, Prospects and Future. *J. Power Sources* **2010**, *195*, 2419−2430.

(2) Etacheri, V.; Marom, R.; Elazari, R.; Salitra, G.; Aurbach, D. Challenges in the Development of Advanced Li-Ion Batteries: A Review. *Energy Environ. Sci.* **2011**, *4*, 3243−3262.

(3) Andre, D.; Hain, H.; Lamp, P.; Maglia, F.; Stiaszny, B. Future High-Energy Density Anode Materials from an Automotive Application Perspective. *J. Mater. Chem. A* **2017**, *5*, 17174−17198.

(4) Huang, C.-K.; Sakamoto, J. S.; Wolfenstine, J.; Surampudi, S. The Limits of Low-Temperature Performance of Li-Ion Cells. *J. Electrochem. Soc.* **2000**, *147*, 2893−2896.

(5) Riedel, O.; Düttmann, A.; Dühnen, S.; Kolny-Olesiak, J.; Gutsche, C.; Parisi, J.; Winter, M.; Knipper, M.; Placke, T. Surface-Modified Tin Nanoparticles and Their Electrochemical Performance in Lithium Ion Battery Cells. *ACS Appl. Nano Mater.* **2019**, *2*, 3577−3589.

(6) Wang, B.; Ryu, J.; Choi, S.; Zhang, X.; Pribat, D.; Li, X.; Zhi, L.; Park, S.; Ruoff, R. S. Ultrafast-Charging Silicon-Based Coral-Like Network Anodes for Lithium-Ion Batteries with High Energy and Power Densities. *ACS Nano* **2019**, 2307−2315.

(7) Yu, S.-H.; Lee, S. H.; Lee, D. J.; Sung, Y.-E.; Hyeon, T. Conversion Reaction-Based Oxide Nanomaterials for Lithium Ion Battery Anodes. *Small* **2016**, *12*, 2146−2172.

(8) Permien, S.; Indris, S.; Hansen, A.-L.; Scheuermann, M.; Zahn, D.; Schürmann, U.; Neubüser, G.; Kienle, L.; Yegudin, E.; Bensch, W. Elucidation of the Conversion Reaction of $CoMnFeO_4$ Nanoparticles in Lithium Ion Battery Anode via Operando Studies. *ACS Appl. Mater. Interfaces* **2016**, *8*, 15320−15332.

(9) Bresser, D.; Passerini, S.; Scrosati, B. Leveraging Valuable Synergies by Combining Alloying and Conversion for Lithium-Ion Anodes. *Energy Environ. Sci.* **2016**, *9*, 3348−3367.

(10) Mueller, F.; Gutsche, A.; Nirschl, H.; Geiger, D.; Kaiser, U.; Bresser, D.; Passerini, S. Iron-Doped ZnO for Lithium-Ion Anodes: Impact of the Dopant Ratio and Carbon Coating Content. *J. Electrochem. Soc.* **2017**, *164*, A6123−A6130.

(11) Giuli, G.; Trapananti, A.; Mueller, F.; Bresser, D.; D'Acapito, F.; Passerini, S. Insights into the Effect of Iron and Cobalt Doping on the Structure of Nanosized ZnO. *Inorg. Chem.* **2015**, *54*, 9393−9400.

(12) Ulissi, U.; Elia, G. A.; Jeong, S.; Mueller, F.; Reiter, J.; Tsiouvaras, N.; Sun, Y.-K.; Scrosati, B.; Passerini, S.; Hassoun, J. Low-Polarization Lithium-Oxygen Battery Using [DEME][TFSI] Ionic Liquid Electrolyte. *ChemSusChem* **2018**, *11*, 229−236.

(13) Cabo-Fernandez, L.; Bresser, D.; Braga, F.; Passerini, S.; Hardwick, L. J. In-Situ Electrochemical SHINERS Investigation of SEI Composition on Carbon-Coated $Zn_{0.9}Fe_{0.1}O$ Anode for Lithium-Ion Batteries. *Batteries Supercaps* **2019**, *2*, 168−177.

(14) Giuli, G.; Eisenmann, T.; Bresser, D.; Trapananti, A.; Asenbauer, J.; Mueller, F.; Passerini, S. Structural and Electrochemical Characterization of $Zn_{1-x}Fe_xO$—Effect of Aliovalent Doping on the Li+ Storage Mechanism. *Materials* **2017**, *11*, No. 49.

(15) Bresser, D.; Mueller, F.; Fiedler, M.; Krueger, S.; Kloepsch, R.; Baither, D.; Winter, M.; Paillard, E.; Passerini, S. Transition-Metal-Doped Zinc Oxide Nanoparticles as a New Lithium-Ion Anode Material. *Chem. Mater.* **2013**, *25*, 4977−4985.

(16) Meister, P.; Jia, H.; Li, J.; Kloepsch, R.; Winter, M.; Placke, T. Best Practice: Performance and Cost Evaluation of Lithium Ion Battery Active Materials with Special Emphasis on Energy Efficiency. *Chem. Mater.* **2016**, *28*, 7203−7217.

(17) Kobayashi, Y.; Miyashiro, H.; Kumai, K.; Takei, K.; Iwahori, T.; Uchida, I. Precise Electrochemical Calorimetry of $LiCoO_2$/Graphite Lithium-Ion Cell. *J. Electrochem. Soc.* **2002**, *149*, A978−A982.

(18) Kobayashi, Y.; Kihira, N.; Takei, K.; Miyashiro, H.; Kumai, K.; Terada, N.; Ishikawa, R. Electrochemical and Calorimetric Approach to Spinel Lithium Manganese Oxide. *J. Power Sources* **1999**, *81*−*82*, 463−466.

(19) Kobayashi, Y.; Mita, Y.; Seki, S.; Ohno, Y.; Miyashiro, H.; Nakayama, M.; Wakihara, M. Configurational Entropy of Lithium Manganese Oxide and Related Materials, $LiCr_yMn_{2-y}O_4$ (Y=0, 0.3). *J. Electrochem. Soc.* **2008**, *155*, A14−A19.

(20) Lu, W.; Belharouak, I.; Park, S. H.; Sun, Y. K.; Amine, K. Isothermal Calorimetry Investigation of $Li_{1+x}Mn_{2-y}Al_zO_4$ Spinel. *Electrochim. Acta* **2007**, *52*, 5837−5842.

(21) Kobayashi, Y.; Tabuchi, M.; Miyashiro, H.; Kuriyama, N. A New Design of Highly Reversible $LiNiO_2$: Defect Formation in Transition Metal Site. *J. Power Sources* **2017**, *364*, 156−162.

(22) van Bommel, A.; Krause, L. J.; Dahn, J. R. Investigation of the Irreversible Capacity Loss in the Lithium-Rich Oxide Li-$[Li_{1/5}Ni_{1/5}Mn_{3/5}]O_2$. *J. Electrochem. Soc.* **2011**, *158*, A731−A735.

(23) Lu, W.; Belharouak, I.; Vissers, D.; Amine, K. In Situ Thermal Study of $Li_{1+x}[Ni_{1/3}Co_{1/3}Mn_{1/3}]_{1-x}O_2$ Using Isothermal Micro-Clorimetric Techniques. *J. Electrochem. Soc.* **2006**, *153*, A2147−A2151.

(24) Yang, H.; Prakash, J. Determination of the Reversible and Irreversible Heats of a $LiNi_{0.8}Co_{0.15}Al_{0.05}O_2$/Natural Graphite Cell Using Electrochemical-Calorimetric Technique. *J. Electrochem. Soc.* **2004**, *151*, A1222−A1229.

(25) Lu, W.; Yang, H.; Prakash, J. Determination of the Reversible and Irreversible Heats of $LiNi_{0.8}Co_{0.2}O_2$/Mesocarbon Microbead Li-Ion Cell Reactions Using Isothermal Microcalorimetery. *Electrochim. Acta* **2006**, *51*, 1322−1329.

(26) Lu, W.; Prakash, J. In Situ Measurements of Heat Generation in a Li/Mesocarbon Microbead Half-Cell. *J. Electrochem. Soc.* **2003**, *150*, A262−A266.

(27) Lu, W.; Belharouak, I.; Liu, J.; Amine, K. Thermal Properties of $Li_{4/3}Ti_{5/3}O_4/LiMn_2O_4$ Cell. *J. Power Sources* **2007**, *174*, 673−677.

(28) Glazier, S. L.; Li, J.; Louli, A. J.; Allen, J. P.; Dahn, J. R. An Analysis of Artificial and Natural Graphite in Lithium Ion Pouch Cells Using Ultra-High Precision Coulometry, Isothermal Microcalorimetry, Gas Evolution, Long Term Cycling and Pressure Measurements. *J. Electrochem. Soc.* **2017**, *164*, A3545−A3555.

(29) Glazier, S. L.; Downie, L. E.; Xia, J.; Louli, A. J.; Dahn, J. R. Effects of Fluorinated Carbonate Solvent Blends on High Voltage

Parasitic Reactions in Lithium Ion Cells Using OCV Isothermal Microcalorimetry. *J. Electrochem. Soc.* **2016**, *163*, A2131−A2138.
(30) Downie, L. E.; Hyatt, S. R.; Dahn, J. R. The Impact of Electrolyte Composition on Parasitic Reactions in Lithium Ion Cells Charged to 4.7 V Determined Using Isothermal Microcalorimetry. *J. Electrochem. Soc.* **2016**, *163*, A35−A42.
(31) Downie, L. E.; Nelson, K. J.; Petibon, R.; Chevrier, V. L.; Dahn, J. R. The Impact of Electrolyte Additives Determined Using Isothermal Microcalorimetry. *ECS Electrochem. Lett.* **2013**, *2*, A106−A109.
(32) Downie, L. E.; Dahn, J. R. Determination of the Voltage Dependence of Parasitic Heat Flow in Lithium Ion Cells Using Isothermal Microcalorimetry. *J. Electrochem. Soc.* **2014**, *161*, A1782−A1787.
(33) Seo, J.; Sankarasubramanian, S.; Kim, C.-S.; Hovington, P.; Prakash, J.; Zaghib, K. Thermal Characterization of Li/Sulfur, Li/ S−$LiFePO_4$ and Li/S−LiV_3O_8 Cells Using Isothermal Micro-Calorimetry and Accelerating Rate Calorimetry. *J. Power Sources* **2015**, *289*, 1−7.
(34) Huie, M. M.; Bock, D. C.; Wang, L.; Marschilok, A. C.; Takeuchi, K. J.; Takeuchi, E. S. Lithiation of Magnetite (Fe_3O_4): Analysis Using Isothermal Microcalorimetry and Operando X-Ray Absorption Spectroscopy. *J. Phys. Chem. C* **2018**, *122*, 10316−10326.
(35) Huie, M. M.; Bock, D. C.; Bruck, A. M.; Tallman, K. R.; Housel, L. M.; Wang, L.; Thieme, J.; Takeuchi, K. J.; Takeuchi, E. S.; Marschilok, A. C. Isothermal Microcalorimetry: Insight into the Impact of Crystallite Size and Agglomeration on the Lithiation of Magnetite, Fe_3O_4. *ACS Appl. Mater. Interfaces* **2019**, *11*, 7074−7086.
(36) Bresser, D.; Paillard, E.; Kloepsch, R.; Krueger, S.; Fiedler, M.; Schmitz, R.; Baither, D.; Winter, M.; Passerini, S. Carbon Coated $ZnFe_2O_4$ Nanoparticles for Advanced Lithium-Ion Anodes. *Adv. Energy Mater* **2013**, *3*, 513−523.
(37) Martinez-Julian, F.; Guerrero, A.; Haro, M.; Bisquert, J.; Bresser, D.; Paillard, E.; Passerini, S.; Garcia-Belmonte, G. Probing Lithiation Kinetics of Carbon-Coated $ZnFe_2O_4$ Nanoparticle Battery Anodes. *J. Phys. Chem. C* **2014**, *118*, 6069−6076.
(38) Becker, S. M.; Scheuermann, M.; Sepelák, V.; Eichhöfer, A.; Chen, D.; Mönig, R.; Ulrich, A. S.; Hahn, H.; Indris, S. Electrochemical Insertion of Lithium in Mechanochemically Synthesized Zn_2SnO_4. *Phys. Chem. Chem. Phys.* **2011**, *13*, 19624−19631.
(39) Grey, C. P.; Dupré, N. NMR Studies of Cathode Materials for Lithium-Ion Rechargeable Batteries. *Chem. Rev.* **2004**, *104*, 4493−4512.
(40) Giuli, G.; Trapananti, A.; Mueller, F.; Bresser, D.; Dácapito, F.; Passerini, S. Insights into the Effect of Iron and Cobalt Doping on the Structure of Nanosized ZnO. *Inorg. Chem.* **2015**, *54*, 9393−9400.
(41) Stewart, S. J.; Figueroa, S. J. A.; Sturla, M. B.; Scorzelli, R. B.; García, F.; Requejo, F. G. Magnetic $ZnFe_2O_4$ Nanoferrites Studied by X-Ray Magnetic Circular Dichroism and Mössbauer Spectroscopy. *Phys. B* **2007**, *389*, 155−158.
(42) Ehrhardt, H.; Campbell, S. J.; Hofmann, M. Magnetism of the Nanostructured Spinel Zinc Ferrite. *Scr. Mater.* **2003**, *48*, 1141−1146.
(43) MacEachern, L.; Dunlap, R. A.; Obrovac, M. N. Li-Ion Battery Negative Electrodes Based on the Fe_xZn_{1-x} Alloy System. *J. Non-Cryst. Solids* **2015**, *409*, 183−190.
(44) Bernardi, D.; Pawlikowski, E.; Newman, J. Newman − A General Energy Balance for Battery Systems. *J. Electrochem. Soc.* **1985**, *132* (1), 5−12.
(45) Ko, J. K.; Wiaderek, K. M.; Pereira, N.; Kinnibrugh, T. L.; Kim, J. R.; Chupas, P. J.; Chapman, K. W.; Amatucci, G. G. Transport, Phase Reactions, and Hysteresis of Iron Fluoride and Oxyfluoride Conversion Electrode Materials for Lithium Batteries. *ACS Appl. Mater. Interfaces* **2014**, *6*, 10858−10869.
(46) Krause, L. J.; Jensen, L. D.; Dahn, J. R. Measurement of Parasitic Reactions in Li Ion Cells by Electrochemical Calorimetry. *J. Electrochem. Soc.* **2012**, *159*, A937−A943.
(47) Obrovac, M. N.; Chevrier, V. L. Alloy Negative Electrodes for Li-Ion Batteries. *Chem. Rev.* **2014**, *114*, 11444−11502.
(48) Rezvani, S. J.; Gunnella, R.; Witkowska, A.; Mueller, F.; Pasqualini, M.; Nobili, F.; Passerini, S.; Cicco, A. D. Is the Solid Electrolyte Interphase an Extra-Charge Reservoir in Li-Ion Batteries? *ACS Appl. Mater. Interfaces* **2017**, *9*, 4570−4576.
(49) Ponrouch, A.; Taberna, P.-L.; Simon, P.; Palacín, M. R. On the Origin of the Extra Capacity at Low Potential in Materials for Li Batteries Reacting through Conversion Reaction. *Electrochim. Acta* **2012**, *61*, 13−18.
(50) Bresser, D.; Paillard, E.; Kloepsch, R.; Krueger, S.; Fiedler, M.; Schmitz, R.; Baither, D.; Winter, M.; Passerini, S. Carbon Coated $ZnFe_2O_4$ nanoparticles for Advanced Lithium-Ion Anodes. *Adv. Energy Mater.* **2013**, *3*, 513−523.
(51) Ma, Y.; Ulissi, U.; Bresser, D.; Ma, Y.; Ji, Y.; Passerini, S. Manganese Silicate Hollow Spheres Enclosed in Reduced Graphene Oxide as Anode for Lithium-Ion Batteries. *Electrochim. Acta* **2017**, *258*, 535−543.
(52) Ma, Y.; Ma, Y.; Ulissi, U.; Ji, Y.; Streb, C.; Bresser, D.; Passerini, S. Influence of the Doping Ratio and the Carbon Coating Content on the Electrochemical Performance of Co-Doped SnO_2 for Lithium-Ion Anodes. *Electrochim. Acta* **2018**, *277*, 100−109.
(53) Barroso-Bogeat, A.; Alexandre-Franco, M.; Fernández-González, C.; Macías-García, A.; Gómez-Serrano, V. Electrical Conductivity of Activated Carbon−Metal Oxide Nanocomposites under Compression: A Comparison Study. *Phys. Chem. Chem. Phys.* **2014**, *16*, 25161−25175.
(54) Ma, Y.; Ma, Y.; Giuli, G.; Diemant, T.; Behm, R. J.; Geiger, D.; Kaiser, U.; Ulissi, U.; Passerini, S.; Bresser, D. Conversion/Alloying Lithium-Ion Anodes—Enhancing the Energy Density by Transition Metal Doping. *Sustainable Energy Fuels* **2018**, *2*, 2601−2608.